A Computational Design Tool for Compliant Mechanisms

VITTORIO MEGARO, ETH Zurich, Disney Research
JONAS ZEHNDER, Disney Research
MORITZ BÄCHER, Disney Research
STELIAN COROS, Carnegie Mellon University
MARKUS GROSS, Disney Research
BERNHARD THOMASZEWSKI, Disney Research

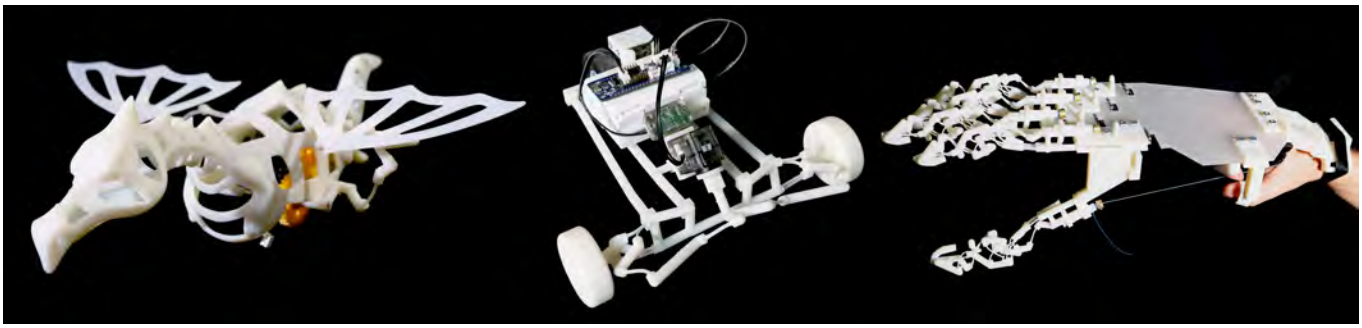

Fig. 1. Our computational tool for designing compliant mechanisms allows non-expert users to generate compliant versions of conventional, rigidly-articulated mechanisms. As we demonstrate with a diverse set of examples ranging from a spatial wing (left) and steering mechanism (middle) to a compliant hand well-suited for teleoperation tasks (right), our technique leads to structurally-sound and function-preserving compliant designs.

We present a computational tool for designing compliant mechanisms. Our method takes as input a conventional, rigidly-articulated mechanism defining the topology of the compliant design. This input can be both planar or spatial, and we support a number of common joint types which, whenever possible, are automatically replaced with parameterized flexures. As the technical core of our approach, we describe a number of objectives that shape the design space in a meaningful way, including trajectory matching, collision avoidance, lateral stability, resilience to failure, and minimizing motor torque. Optimal designs in this space are obtained as solutions to an equilibrium-constrained minimization problem that we solve using a variant of sensitivity analysis. We demonstrate our method on a set of examples that range from simple four-bar linkages to full-fledged animatronics, and verify the feasibility of our designs by manufacturing physical prototypes.

CCS Concepts: • **Computer graphics → Computational geometry and object modeling**; *Physically based modeling*;

ACM Reference format:
Vittorio Megaro, Jonas Zehnder, Moritz Bächer, Stelian Coros, Markus Gross, and Bernhard Thomaszewski. 2017. A Computational Design Tool for Compliant Mechanisms. *ACM Trans. Graph.* 36, 4, Article 82 (July 2017), 12 pages.
https://doi.org/http://dx.doi.org/10.1145/3072959.3073636

0730-0301/2017/7-ART82 $15.00
https://doi.org/http://dx.doi.org/10.1145/3072959.3073636

1 INTRODUCTION

Engineers routinely design for strength and stiffness. Steel and concrete prevent deflections in buildings, and machines resort to rigid articulation in order to avoid deformations. But although most human designs are inspired by Nature, rigidity is a concept foreign to the living world: from a kangaroo's legs to the wings of a bat—bones, tendons, and cartilage are the nuts and bolts of organic machines, and deformation is an integral part of the design, crucial for both efficiency and robustness. Unfortunately, designing for flexibility requires deep understanding and precise predictions of finite deformations, which proves to be substantially more difficult than relying on rigidity.

Fueled by progress in technology and computation, however, many fields of engineering have started to *embrace deformation* and to leverage flexibility for better, more elegant, and ultimately more satisfying designs. Applied to machines, this turn to the flexible leads to *compliant mechanisms*, i.e., mechanical devices that perform motion not through rigid articulation but by virtue of elastically deforming flexures. Compliant mechanisms enjoy widespread use in industry, where they are valued for their accuracy, ease of manufacturing, scalability, and cost efficiency. The spectrum ranges from specialized microelectromechanical systems (MEMS) for miniature sensors and actuators [Kota et al. 2001], to more mundane devices including monolithic pliers and wiper blades, and to commonplace products such as binder clips, backpack latches, and shampoo lids.

We are primarily interested in exploring the potential of compliant mechanisms for personalized automata and animatronics. With the ability to create complex geometry and its repertoire of flexible, plastic-like materials, 3D printing is an ideal way of manufacturing

compliant mechanisms. And thanks to the increasing availability of consumer-level printers, hobbyist mechanics and other non-expert users now have the machinery to create compliant mechanisms for use in their conceptions and contraptions. But perhaps even more than for conventional mechanisms, the path to a successful compliant design is littered with traps for the novice:

- Compliant mechanisms typically involve large deflections that give rise to nonlinearities in both geometry and material behavior, not rarely betraying intuition.
- For conventional mechanisms, the resistance to motion is either zero or infinite. In the compliant setting, any motion requires a finite amount of work and, depending on direction, the stiffness can vary by orders of magnitude. Shaping the corresponding energy landscape, i.e., finding a balance between stiffness and flexibility is one central aspect of this design problem.
- Compliant mechanisms provide friction- and wear-less motion, but incautious design can induce material fatigue and failure. In order to minimize this risk, high stress concentrations must be avoided.
- While the *forward* problem of predicting the motion of a compliant mechanism is a non-trivial task already, the *inverse* problem of determining parameter values that lead to a desired motion or function is extremely difficult.

Considering these challenges, designing compliant mechanisms is all but a hopeless endeavor for casual users.

Overview & Contributions. We propose an assistive tool that enables non-expert users to leverage the advantages of compliant mechanisms while avoiding common pitfalls. In line with recent work on fabrication-oriented design, we rely on simulation and optimization technology in order to automate technically difficult tasks as much as possible. To this end, we adopt the so called pseudo-rigid-body model [Howell and Midha 1994] as a basis and represent compliant mechanisms as sets of rigid links connected by elastic flexures. Our method takes as input a conventional, rigidly-articulated mechanism defining the topology of the compliant design. This input can be both planar or spatial, and we support a number of common joint types which, whenever possible, are automatically replaced with flexures drawn from existing catalogs [Howell et al. 2013; Smith 2000]. As the technical core of our approach, we describe a number of objectives that shape the design space in a meaningful way. The list of objectives includes trajectory matching, collision avoidance, lateral stability, resilience to failure, and minimizing motor torque. To represent our flexures, we use discrete elastic rods [Bergou et al. 2010, 2008], extending the model to predict *volumetric* stresses. Optimal designs in this space are obtained as solutions to an equilibrium-constrained minimization problem that we solve using a variant of sensitivity analysis. We demonstrate our method on a set of examples that range from simple four-bar linkages to full-fledged animatronics, and verify the feasibility of our designs by manufacturing physical prototypes.

2 RELATED WORK

Fabrication-oriented Design. Driven by technological advances in digital fabrication, the graphics community has devoted a significant effort on the computational design of physical artifacts, characters and structures. Proposed techniques have targeted plush toys [Mori and Igarashi 2007] besides structurally-sound [Lu et al. 2014; Stava et al. 2012; Umetani and Schmidt 2013; Zhou et al. 2013] and stably standing [Prévost et al. 2013], spinning [Bächer et al. 2014], or floating [Musialski et al. 2015] 3D printable models. Diverse design problems including stably flying gliders [Umetani et al. 2014], composition of wire meshes [Garg et al. 2014], thermoforming of shapes [Schüller et al. 2016], and wind instruments [Umetani et al. 2016] have been tackled. Similar to our flexures, fexible rod [Pérez et al. 2015], filigree [Chen et al. 2016], ornamental curve [Zehnder et al. 2016] and stable rod [Miguel et al. 2016] structures are designed to last when bent. Authors have also addressed the design and fabrication of articulated [Bächer et al. 2012; Calì et al. 2012], deformable [Skouras et al. 2013], or inflatable characters [Skouras et al. 2014]. In contrast, we target the design of function-preserving compliant mechanisms, tailored for fabrication with additive manufacturing technologies.

Conventional Mechanism Design. Several techniques that aid the non-expert with the understanding [Mitra et al. 2010], design [Ceylan et al. 2013; Coros et al. 2013; Hergel and Lefebvre 2015; Lin et al. 2016; Thomaszewski et al. 2014; Zhu et al. 2012], editing [Bächer et al. 2015], and recovery [Koo et al. 2014] of complex mechanical assemblies have recently been proposed. The output of these approaches serve as input to our technique. While we do not support the conversion of joints with relative motion such as, e.g., prismatic joints [Coros et al. 2013], the user has the option to convert a subset of conventional to compliant joints, keeping the remaining ones unchanged. Hence, our system is versatile.

Compliant Mechanism Synthesis. Compliant mechanisms achieve motion through elastic deformation and have been the subject matter of a large body of prior art. An exhaustive review is beyond the scope of this paper and we focus our discussion on mechanism synthesis, referring the interested reader to excellent books [Howell 2001; Howell et al. 2013; Smith 2000] and a recent survey [Albanesi et al. 2010] on the subject matter.

Early synthesis techniques used structural optimization [Kota and Ananthasuresh 1995] that bear the advantage of supporting topological changes. While initially targeting planar mechanisms, follow-up work [Frecker et al. 1997] addresses the design of compliant spatial mechanisms. Wang et al. [2009] propose a stiffness matrix representation and target synthesis of planar mechanisms through topology optimization. Like these works, we account for kinematic and structural requirements in the design process. However, we base our formulation on elastic rods [Bergou et al. 2010, 2008] instead of beam deflection theory [Frecker et al. 1997; Kota and Ananthasuresh 1995] or small-displacement analysis [Wang and Chen 2009], significantly increasing the prediction quality for large deformations and a non-linear behavior.

Related to our effort is pseudo-rigid-body replacement [Howell and Midha 1994]. Like in our approach, a designer starts with a conventional mechanism designed to accomplish a particular task. Conventional joints are then replaced with torsional springs to provide an expert designer with approximate performance estimates. She then replaces conventional joints one-by-one, adjusting torsional

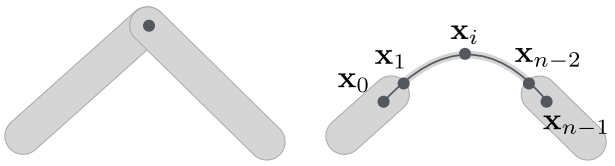

Fig. 2. **Conventional vs. compliant hinge.** We replace conventional joints (left) with a single or several flexures (right).

spring constants of the pseudo-rigid-body model. We automate this process and avoid an overly simplified elasticity model and a tedious manual tuning of spring constants.

To provide the compliant mechanism designer with guidelines on the placement and orientation of flexures, Hopkins et al. [2010a; 2010b] developed the concept of Freedom and Constraint Topology (FACT) with theoretical underpinnings in screw theory [Huang et al. 2013]. We follow these guidelines when replacing conventional joints, favoring compliance in desired and stiffness in undesired directions.

Limaye et al. [2012] propose a kit with flexible beams and connectors together with an analysis and synthesis approach to design and hand-assemble compliant mechanisms. While restricted to the plane, their synthesis enables rapid design iterations of monolithic compliant mechanisms. The design space, however, is restricted, supporting only beams of discrete length and a single connector type.

3 COMPUTATIONAL MODEL

The core of our method is formed by a computational model that allows us to simulate the behavior of a given compliant mechanism design (Sec. 3.1). The design itself is described in terms of a dedicated flexure-centric parameterization (Sec. 3.2), defining the interface to subsequent optimization (Sec. 4).

3.1 Simulating Compliant Mechanisms

We model compliant mechanisms as sets of rigid links interconnected by flexible joints. The state of each rigid link is represented as a vector $\mathbf{s}_i \in \mathbb{R}^6$ holding translational and rotational degrees of freedom. Each compliant joint is composed of a set of flexures—thin lamella which we model using discrete elastic rods [Bergou et al. 2010, 2008]. A flexure is represented by a piece-wise linear centerline, given as a set of vertices $\mathbf{x}_i$, as well as a set of radii, a_j and b_j, defining the width and height of the elliptical cross section for each edge of the centerline.

In addition to compliant flexures, our approach also supports conventional joints, which are used, e.g., when full revolutions are required. Following Coros and colleagues [2013] we model conventional joints using simple geometric constraints $\mathbf{C}(\mathbf{s})$.

Our compliant mechanisms are actuated by connecting one or several of the rigid links to an input driver such as a motor or a crank. In order to obtain proper two-way coupling, we ask that the first and last two centerline vertices (compare with Fig. 2 right) move rigidly with the incident links $\mathbf{s}_i$ and $\mathbf{s}_j$, which we implement by eliminating the corresponding degrees of freedom. The motion of the input link then propagates throughout the mechanism, causing flexures to stretch, bend, and twist. These deformations give rise to internal energy $E_{\text{int}}(\mathbf{x})$ that is computed according to [Bergou et al. 2008].

Given the states of all input links, we can compute the equilibrium configuration of the mechanism by solving the constrained optimization problem

$$\min_{\mathbf{x},\mathbf{s}} \; E_{\text{int}}(\mathbf{p},\mathbf{x},\mathbf{s}) \quad \text{s.t.} \quad \mathbf{C}(\mathbf{p},\mathbf{s}) = \mathbf{0}\,, \tag{1}$$

where $\mathbf{x}$ and $\mathbf{s}$ collect the degrees of freedom of all flexures and links, respectively, and $\mathbf{p}$ is a vector of design parameters, defining the rest state of the mechanism as described next.

3.2 Parameterizing Compliant Joints

Given a conventional mechanism as input, our goal is to replace rigidly-articulated joints with compliant counterparts wherever possible and desired. To this end, we can in principle choose from existing catalogs [Howell et al. 2013] that provide designs for many types of conventional joints, typically with several alternatives for each type. When choosing a particular compliant joint, we ask that the range of motion of the original joint be preserved as much as possible, including degrees of freedom as well as constraints. Moreover, we would like the compliant joints to be readily parameterized and easy to manufacture.

Revolute Joints. As the most frequently found joint in planar and spatial linkages, hinges can, in principle, be modeled using only a single flexure. By choosing an elliptical cross section that is wide along the rotation axis $\mathbf{a}_i$ of the original joint, but thin in the orthogonal direction, high lateral stability can be achieved with small in-plane stiffness. However, the ratio between in-plane compliance and out-of-plane stiffness of a design with multiple antagonistic (i.e., 'crossing') flexures can be significantly higher for the same total width. We therefore adopt a layered flexure design that, as illustrated in Fig. 3, consists of two flexures stacked along $\mathbf{a}_i$. In order to allow for smooth geometry with a minimum number of parameters, we model each flexure as a cubic Hermite spline, defined by two end points $\mathbf{q}_j$ and corresponding tangent vectors $\mathbf{t}_j$. The flexure is required to remain within its layer, which we achieve by using polar coordinates to parameterize the attachment points with respect to the location $\mathbf{r}_i$ of the original joint as

$$\mathbf{q}_j = \mathbf{r}_i + r_j(\cos\phi_j \mathbf{e}_1 + \sin\phi_j \mathbf{e}_2)\,. \tag{2}$$

In the above expression, r_j and ϕ_j are radial and angular coordinates as illustrated in Fig. 3 (top, middle) and (top, right), and $[\mathbf{e}_1, \mathbf{e}_2]$ span the plane orthogonal to $\mathbf{a}_i$. Tangent vectors are described analogously (bottom, left) and (bottom, middle), and two additional parameters control the distance between the attachment points of the two flexures on the same link, such as to create, e.g., cross

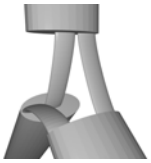

configurations with high lateral stability (Fig. 3, bottom right). The layered design also generalizes readily to hinge joints connecting more than two components as illustrated in the inset on the left with a three-way coupling, where an additional layer is required to accommodate all three flexures.

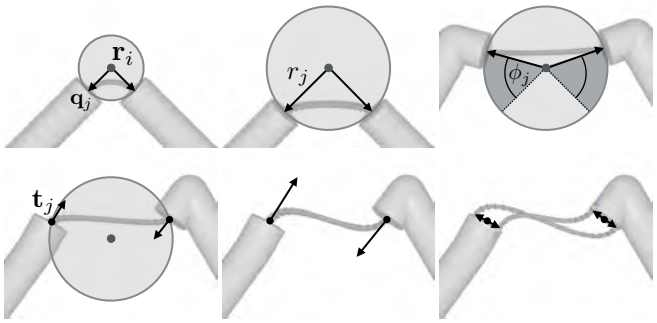

Fig. 3. Parameterizing a compliant hinge with two offset flexures.

Other Joint Types. For spherical joints, we use a single flexure with circular cross section (compare with Fig. 4 left), offering comparatively low resistance to bending and twisting deformation, but orders of magnitude higher stiffness for stretching. Similar to hinge joints, flexures for spherical joints are modeled as spline curves whose attachment points are required to remain within a certain spherical volume relative to the original joint location.

In addition to revolute and spherical joints, compliant universal joints can be modeled as well using, e.g., two flexures with mutually orthogonal axes connected serially as illustrated in Fig. 4 (right). These three joint types allow us to create a large and diverse set of meaningful linkages and other mechanical assemblies. Note that connections involving translational motion are inherently difficult to achieve using compliant joints. However, our formulation supports rigidly-articulated versions of these joints, both in terms of simulation and optimization.

3.3 Generating Link Geometry

With a view to design optimization, we collect the parameters of all flexures in a vector $\mathbf{p}$. Taken together, these parameters completely define the undeformed configuration of the compliant mechanism. In particular, they define the rest state geometries for all flexures which, in turn, determine the behavior of the mechanism. In order to obtain a functional, printable mechanism, we have to generate geometry for all rigid links, and this geometry should automatically adapt to changes in the flexure parameters during optimization. To this end, we represent the geometry for each link as a union of capsules, a representation that is readily parameterized and simplifies collision tests (see Sec. 4.4). More concretely, we model each link as a union of three cylinders and two spheres, as illustrated in the inset figure. Two of the cylinders have fixed lengths and attach to the flexures on either side of the link. These two cylinders are, in turn, connected by a third cylinder of variable length, and we place spheres at the corresponding intersection points in order to obtain smooth transitions. Though simple, this procedural link geometry has the advantage that derivatives with respect to flexure parameters, which are required for design optimization, are readily computed.

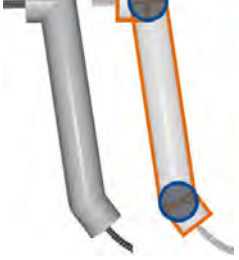

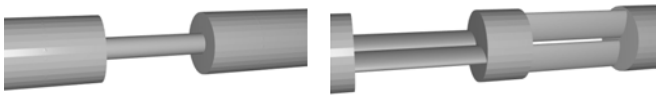

Fig. 4. Compliant ball-and-socket (left) and universal joint (right).

4 DESIGN OPTIMIZATION

Given an initial design for a compliant mechanism, we seek to find parameter values for all flexures such as to optimize the function of the mechanism with respect to various objectives, including motion tracking, ease of actuation, and resilience to failure. We first introduce the individual objectives, then describe how to compute optimal parameter values.

4.1 Motion Tracking

Generating motion is a central function of both conventional and compliant mechanisms. For example, it is crucial for the end effector in a compliant leg mechanism to closely follow the corresponding trajectory of the conventional counterpart in order to ensure proper walking. Similarly, the finger of a compliant robot hand needs to offer the same range of motion to successfully perform grasping tasks. In order to encourage accurate motion approximation, we introduce a trajectory matching objective of the form

$$f_{\text{track}} = \frac{1}{2} \sum_t \|\mathbf{z}_t(\mathbf{x}_t, \mathbf{s}_t) - \hat{\mathbf{z}}_t\|^2 , \tag{3}$$

where $\mathbf{z}_t$ describes the discrete trajectory of a point on the compliant mechanism, and $\hat{\mathbf{z}}_t$ is the corresponding target trajectory on the input mechanism. In order to evaluate the tracking objective, we step through a full motion cycle or along a user-specified animation and compute the corresponding equilibrium states $(\mathbf{x}_t, \mathbf{s}_t)$ by minimizing (1).

4.2 Lateral Stability

A conventional mechanism exhibits zero resistance to motion corresponding to its degrees of freedom, and infinite stiffness in all orthogonal directions. However, this crisp picture becomes somewhat blurred for compliant mechanisms, which exhibit finite resistance to motion in all directions. In particular, instead of deriving from a degree of freedom, the motion of a compliant mechanism is a path through an energy landscape, lined with preferably steep walls to the sides, but sloping rather gently along its direction. Low resistance to motion along this path is desirable as this leads to less stringent torque requirements. While some amount of compliance perpendicular to the trajectory can be desirable as well (e.g., for grasping or walking), a certain minimum stiffness to lateral motion is always required. One particular way of encouraging lateral stability is to apply a given force $\mathbf{f}_l$ to the mechanism and ask that the resulting displacement be minimal or bounded. Using the motion tracking objective (3) as a basis, the deviation from the original trajectory can be expressed as

$$f_{\text{stab}} = \frac{1}{2} \sum_t \|\mathbf{z}_t(\mathbf{x}_t, \mathbf{s}_t) - \tilde{\mathbf{z}}_t(\mathbf{x}_t, \mathbf{s}_t)\|^2 , \tag{4}$$

where $\tilde{\mathbf{z}}_t$ is the trajectory obtained under the action of $\mathbf{f}_\mathrm{l}$. We generally apply $\mathbf{f}_\mathrm{l}$ at the end effector in a direction approximately normal to the trajectory, but the user is free to change this direction if desired.

4.3 Actuation Requirements

Actuating a compliant mechanism to a given target configuration requires work, holding the position requires torque. Ideally, we would like to minimize the maximum required torque along the trajectory, as this will allow for more precise actuation and for using smaller, less expensive motors. The torque required to hold a compliant mechanism in a given position is equal to the derivative of its elastic energy with respect to the motor angle. Using central differences, we approximate the torque required to sustain a given configuration $(\mathbf{x}_t, \mathbf{s}_t)$ as

$$\tau_t = \frac{1}{\Delta\alpha_t}\left(E(\mathbf{x}_{t+1}, \mathbf{s}_{t+1}) - E(\mathbf{x}_{t-1}, \mathbf{s}_{t-1})\right) , \tag{5}$$

where $\Delta\alpha_t$ is the corresponding change in motor angle. In order to minimize torque requirements, we define an objective function as

$$f_\mathrm{act} = \frac{\sum_t \tau_t^2 e^{\beta_\mathrm{act}\tau_t^2}}{\sum_t e^{\beta_\mathrm{act}\tau_t^2}}, \tag{6}$$

where we set β_act to a large positive value.

4.4 Avoiding Collisions

In order to ensure proper functioning of the mechanism, we have to avoid collisions between its individual links and flexures. There are three cases that need to be handled: flexure-flexure, link-link, and flexure-link collisions. In order to prevent flexure-flexure intersections, we measure the distance between all pairs of edges of the two centerlines. Whenever the distance $d(\mathbf{e}_i, \mathbf{e}_j)$ between two edges $\mathbf{e}_i$ and $\mathbf{e}_j$ is less than a minimum distance d_min, we construct a penalty function of the form

$$f_\mathrm{coll} = \left(\frac{d_\mathrm{min}^2 - d(\mathbf{e}_i, \mathbf{e}_j)^2}{d_\mathrm{min}^2}\right)^3 , \tag{7}$$

that, by construction, has continuous second derivatives at $d = d_\mathrm{min}$. While we could have used an exponential barrier for the penalty function, we found the polynomial version to be sufficient in practice, preventing intersections reliably. For the link-link case, we test all pair-wise combinations of spheres and cylinders and, whenever too close proximity is detected, activate a corresponding penalty term. Finally, in order to prevent intersections between links and flexures, we test each edge of the centerline against the five shapes of the link and issue a penalty term if distances are too small. It should be pointed out that we do not check for flexure-link collisions if the flexure is attached to the link. We found that doing so gives the mechanisms more freedom to adapt at the cost of sometimes introducing collisions; see Fig. 5. These can, however, always be resolved by adapting the geometry of the link in a post-processing step (right). Finally, each of the three cases is implemented using the same closed-form function for measuring the distance between two capsules [Zehnder et al. 2016].

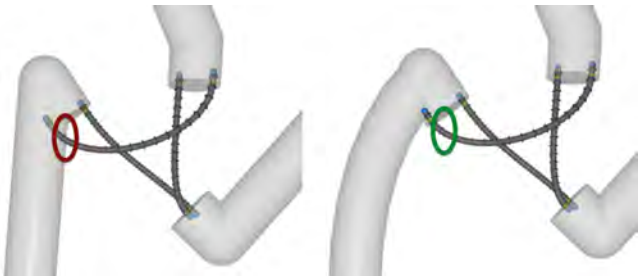

Fig. 5. A collision between a flexure and a link (*left*) is resolved by reshaping the corresponding geometry (*right*).

4.5 Preventing Material Failure

The flexures in a compliant mechanism are only elastic within a certain range of deformation, beyond which material fatigue and, ultimately, failure will occur. One central goal of our approach is to minimize the risk of such failures. The field of fracture mechanics has many ways of modeling various failure modes for different types of materials. One widely used model is the so called von Mises criterion [Hill 1998], which states that the onset of failure—or yielding—is a function of the internal stress acting inside the material. Indeed, many manufacturers provide data for their printable materials that can readily be used in this criterion. But unfortunately, the volumetric stresses required to evaluate the yield criterion are not directly available from the discrete rod model. Our goal is therefore to transform the discrete centerline stretch, bending, and twist into a single volumetric strain tensor, from which the stress is then obtained by virtue of a continuum-mechanics material law.

We base below derivations on the elasticity theory on rods as described in Landau et al. [1986]. For bending, we extend their formulation to curved rest configurations and account for the coupling between stretch and bending away from the centerline. For twist, we largely follow their description, outlining their derivation for the reader's convenience and discussing the interface with the discrete elastic rod model [Bergou et al. 2008].

Volumetric Strain from Bending. In the Kirchhoff-Love model of thin elastic rods, the different deformation modes are decoupled. In particular, bending does not induce centerline stretch and vice versa. When considering the volumetric picture, however, it is evident that bending will induce compression on one side of the centerline and stretching on the opposite side, even though the centerline itself remains unstretched (see Fig. 6). In order to quantify this deformation, we start with a simple example of an initially straight rod bent into a state of constant curvature $\kappa = 1/R$. Let dz denote a length element along the centerline and let dz' be the length of a corresponding segment at a given location x in the rod, where $-a \leq x \leq a$. Furthermore, let $d\bar{z} = d\bar{z}'$ denote the corresponding lengths in the (straight) undeformed configuration. Since the centerline does not stretch under bending, we have $dz = d\bar{z}$. Due to the constant curvature, we have $\frac{dz'}{(R-x)} = \frac{dz}{R}$ and the deformation follows as

$$\varepsilon_z = \frac{dz' - d\bar{z}'}{d\bar{z}'} = -\frac{x}{R} = -\kappa x . \tag{8}$$

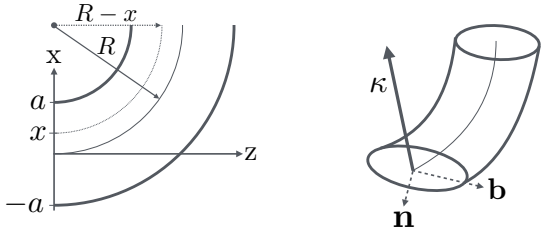

Fig. 6. Bending induces stretching and compression away from the centerline.

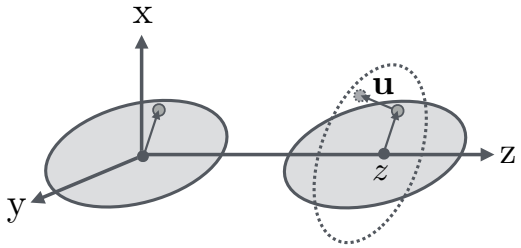

Fig. 7. Twist induces pure shear deformation about the rotation axis.

For curved rest shapes, $dz = d\bar{z}'$ still holds, but additionally we have $\frac{d\bar{z}'}{(\bar{R}-x)} = \frac{d\bar{z}}{\bar{R}}$, where $\bar{R}$ is the radius of curvature for the undeformed state. This leads to

$$\varepsilon_z = -\frac{(\kappa - \bar{\kappa})x}{1 - \bar{\kappa}x} \text{ with } \bar{\kappa} = \frac{1}{\bar{R}} \,. \tag{9}$$

When accounting for simultaneous bending and stretching deformation of the centerline $\varepsilon_{\text{cl}} = \frac{dz}{d\bar{z}} - 1$, we arrive at

$$\varepsilon_z = \frac{\varepsilon_{\text{cl}}(1 - \kappa x) - (\kappa - \bar{\kappa})x}{1 - \bar{\kappa}x} \,. \tag{10}$$

Finally, in order to extend the above formulation to the full three-dimensional picture, we let $\mathbf{c}$ denote an arbitrary point within the elliptical cross section of the rod and write

$$\varepsilon_z(\mathbf{c}) = \frac{\varepsilon_{\text{cl}}(1 - \boldsymbol{\kappa} \cdot \mathbf{c}) - (\boldsymbol{\kappa} - \bar{\boldsymbol{\kappa}}) \cdot \mathbf{c}}{1 - \bar{\boldsymbol{\kappa}} \cdot \mathbf{c}} \tag{11}$$

where $\boldsymbol{\kappa}$ and $\bar{\boldsymbol{\kappa}}$ are 2D vectors holding curvature values relative to the two material directions of the rod. Under the assumption of no shearing [Landau et al. 1986], the bending strain tensor at a given point on the boundary of the cross section is obtained as

$$\boldsymbol{\varepsilon}_b(\mathbf{c}) = \varepsilon_z(\mathbf{c}) \text{diag}\,(-\nu, -\nu, 1) \,, \tag{12}$$

where ν is Poisson's ratio of the material. It is worth noting that $\boldsymbol{\varepsilon}_b$ is a 3×3 tensor expressed relative to the material frame $\mathbf{T} = [\mathbf{t}_1, \mathbf{n}_2, \mathbf{b}_3]$ of the rod, where $\mathbf{n}_1$ and $\mathbf{b}_2$ span the cross-sectional plane and $\mathbf{t}_3$ coincides with its tangent.

To evaluate the strain at vertex i of the discrete elastic rod model (compare with [Bergou et al. 2008]), we first compute the *curvature binormal*, then express it w.r.t. the material frame at i by averaging

$$\mathbf{k}_i = \frac{2\mathbf{t}^{i-1} \times \mathbf{t}^i}{1 + \mathbf{t}^{i-1} \cdot \mathbf{t}^i}, \quad \boldsymbol{\kappa}_i = \frac{1}{2\bar{l}_i} \begin{bmatrix} \mathbf{k}_i \cdot \mathbf{b}^{i-1} + \mathbf{k}_i \cdot \mathbf{b}^i \\ -(\mathbf{k}_i \cdot \mathbf{n}^{i-1} + \mathbf{k}_i \cdot \mathbf{n}^i) \end{bmatrix}$$

with $\left[\mathbf{t}^{i-1}, \mathbf{b}^{i-1}, \mathbf{b}^{i-1}\right]$ and $\left[\mathbf{t}^i, \mathbf{b}^i, \mathbf{b}^i\right]$ denoting the material frames of the two adjacent edges. Note that $\boldsymbol{\kappa}_i$ as defined in Bergou et al. [2008] is an integrated quantity. Hence, we divide by the integration domain $\bar{l}_i$ which equals the sum of the half lengths of the two adjacent, undeformed edges.

Volumetric Strain from Twisting. Analogously to bending, we introduce relevant quantities for twist with an initially straight rod, rotated about the z-axis as depicted in Fig. 7. Focusing our discussion on a cross section parallel to the x-y plane at a small distance z away from the origin, we seek to quantify the displacement a point on the cross section undergoes. To gauge the amount of rotation at z relative to the origin, we multiply z with the the torsion angle τ which measures the angle of rotation per unit length of the rod. We then rotate the cross-sectional point $[x, y, z]^T$ about the z-axis, leading to the in-plane displacement $\mathbf{u}$

$$\begin{bmatrix} -\tau z y \\ \tau z x \\ 0 \end{bmatrix} = \tau z \begin{bmatrix} 0 \\ 0 \\ 1 \end{bmatrix} \times \begin{bmatrix} x \\ y \\ z \end{bmatrix} \,. \tag{13}$$

Cross sections, however, do not stay planar under torsion. To account for out of plane displacement, we follow Landau et al. [1986] and introduce a *torsion function* $\psi(x, y)$ which is cross section dependent

$$\begin{bmatrix} -\tau z y \\ \tau z x \\ \tau \psi(x, y) \end{bmatrix} \tag{14}$$

with the displacement in the z-direction proportional to the torsion angle. This is a sensible choice because for $\tau = 0$ the displacement field is zero.

While significant at global scales, the relative displacement of neighboring points is small under torsion and the linearized Cauchy strain

$$\boldsymbol{\varepsilon}_t(\mathbf{c}) = \frac{1}{2} \begin{bmatrix} 0 & 0 & \tau\left(\frac{\partial \psi}{\partial x} - y\right) \\ 0 & 0 & \tau\left(\frac{\partial \psi}{\partial y} + x\right) \\ \tau\left(\frac{\partial \psi}{\partial x} - y\right) & \tau\left(\frac{\partial \psi}{\partial y} + x\right) & 0 \end{bmatrix}$$

is sufficiently precise. Note that torsion does not lead to any volume changes (diagonal entries are all zero) and is a pure shear deformation, orthogonal to bending and stretching (only diagonal entries non-zero).

For a particular cross section, the torsion function $\psi(x, y)$ is the solution to a Poisson's equation with Neumann boundary conditions that emerges when assuming a linear elastic material

$$\boldsymbol{\sigma}(\mathbf{c}) = \lambda \text{tr}\,(\boldsymbol{\varepsilon}(\mathbf{c}))\,\mathbf{I} + 2\mu\boldsymbol{\varepsilon}(\mathbf{c}) \tag{15}$$

and asking for static equilibrium $\nabla \cdot \boldsymbol{\sigma} = \mathbf{0}$ (see Landau et al. [1986] for a detailed derivation). For an elliptical cross section, the analytical solution is

$$\psi(x, y) = \frac{b^2 - a^2}{a^2 + b^2} xy \,.$$

The torsion angle τ_i at vertex i of the discrete rod model is $\frac{\alpha_i}{\bar{l}_i}$ where α_i is the integrated twist angle at i (see Bergou et al. [2008]).

Failure Criterion. The contributions from centerline stretching, and volumetric bending and twisting are combined into the Cauchy strain $\boldsymbol{\varepsilon}(\mathbf{c}) = \boldsymbol{\varepsilon}_b(\mathbf{c}) + \boldsymbol{\varepsilon}_t(\mathbf{c})$, which we plug into the linear elastic material (Eq. 15) to compute the corresponding Cauchy stress $\boldsymbol{\sigma}(\mathbf{c})$. With the volumetric stress available, we are ready to define a penalty function to prevent material failure. To this end, we ask that the maximum von Mises stress remains below a given threshold value, dictated by the printing material.

Axial strains due to bending and twisting assume their maximum values on the surface of the rod, and so does the corresponding stress. In lack of an analytical expression, we evaluate the stress at a set of n sample points $\mathbf{c}_i = \left\{ \left[a_i \cos(\phi_j) \;\; b_i \sin(\phi_j) \right]^T \right\}$ distributed along the boundary of the cross section, then compute the von Mises stress for sample $\mathbf{c}_j$ as

$$\sigma_v(\mathbf{c}_j) = \sqrt{\frac{3}{2} \sum_{k,l} s_{kl}^2} \text{ and } \mathbf{s}(\mathbf{c}_j) = \boldsymbol{\sigma}(\mathbf{c}_j) - \frac{1}{3}\text{tr}(\boldsymbol{\sigma}(\mathbf{c}_j))\mathbf{I} \,.$$

Finally, the penalty term is defined using the soft maximum over all samples $\mathbf{c}_s^t$ on all rods along the trajectory t,

$$f_{\text{fail}} = \frac{\sum_{t,s} \sigma_v(\mathbf{c}_s^t) e^{\beta_{\text{fail}} \sigma_v(\mathbf{c}_s^t)}}{\sum_{t,s} e^{\beta_{\text{fail}} \sigma_v(\mathbf{c}_s^t)}}, \tag{16}$$

with large positive β_{fail}.

4.6 Optimization

With the design objectives defined, we seek to compute optimal values for all parameters. Since most of these objectives have quite complex derivatives, we first experimented with CMA-ES [Hansen et al. 2003], a widely-used stochastic optimization scheme that does not required derivative information. However, we found the convergence and performance of this algorithm unsatisfying and therefore switched to a more powerful approach based on the implicit function theorem (also known as sensitivity analysis).

To simplify notation, we summarize the system state as $\mathbf{y} = (\mathbf{x}, \mathbf{s})$ and condense all objectives in a single function $f(\mathbf{y})$. In order to compute optimal parameter values, we ask that the gradient of the objective function f vanishes,

$$\frac{\partial f(\mathbf{p}, \mathbf{y}(\mathbf{p}))}{\partial \mathbf{p}} = \mathbf{0} \,, \tag{17}$$

which requires the derivative of state with respect to parameters. To this end, we observe that all admissible states have to be equilibrium configurations, i.e.,

$$\mathbf{g}(\mathbf{p}, \mathbf{y}) = \frac{\partial E(\mathbf{p}, \mathbf{y})}{\partial \mathbf{y}} = \mathbf{0} \,, \tag{18}$$

establishing a map between state and parameters, $\mathbf{y} = \mathbf{y}(\mathbf{p})$. For any admissible changes in parameters, we therefore require that

$$\frac{d\mathbf{g}}{d\mathbf{p}} = \frac{\partial \mathbf{g}}{\partial \mathbf{p}} + \frac{\partial \mathbf{g}}{\partial \mathbf{y}} \frac{\partial \mathbf{y}}{\partial \mathbf{p}} = \mathbf{0} \,, \tag{19}$$

from which we can compute the derivative of state with respect to parameters and, consequently, the gradient of the objective function. We compute the remaining derivatives using a mix of auto-differentiation and manually-derived expressions. For minimization, we use a standard quasi-Newton scheme with L-BFGS [Nocedal 1980].

5 RESULTS

We have used our technique to estimate and fabricate compliant versions for a total of five planar and spatial mechanisms (see Figs. 8-11 and the accompanying video). We minimize a weighted sum of the afore introduced objectives with default values $w_{\text{track}} = 10^5$, $w_{\text{stab}} = 5 \cdot 10^5$, $w_{\text{act}} = 10$, $w_{\text{coll}} = 10^7$, $w_{\text{fail}} = 10^{-6}$ for all our results.

Fabrication and Hardware. For fabrication, we rely on a Stratasys Connex 350 and use their strong and flexible Rigur material. Both rigid links and flexures are printed with the same material and as single assembled pieces. We use Dynamixel's XL-320 and their OpenCM9.04 C-Type board to drive our mechanisms, adding a Robotis BT-210 Bluetooth communication controller for remote control of our RC Car.

Chebyshev Linkage. To analyze the impact of the individual design objectives, we replaced two out of three hinge joints of Chebyshev's Lambda Mechanism with our two-stacked-flexure design while leaving the third one unchanged. Chebyshev's Lambda Mechanism is well-known for its characteristic trajectory with a long, approximately straight segment. As we illustrate in Fig. 8 (top row), we can recover this characteristic trajectory (in blue) from the initially off one (in red) where the average error measured in simulation is lower than a tenth of a millimeter: if only motion tracking of the respective point is active (1st from left), the mechanisms is not fully functional due to a link-link collision. We can prevent this collision while still recovering the trajectory to the same degree (2nd from left) by setting f to $f_{\text{track}} + f_{\text{coll}}$. By further activating f_{act} (3rd from left), we can significantly reduce the required motor torque as we illustrate with before (left column) and after (right column) energy (in blue) and torque profiles (in red) of the cycling motion in the inset on the left. However, while collision-free, the bending and twisting stresses are too high for the targeted printer material. With f_{fail} active (4th from left), we can reduce these stresses by a factor greater than an order of magnitude, resulting in a structurally-sound and functional mechanism. For validation, we fabricated physical prototypes corresponding to designs that were optimized with and without f_{fail}. Using only tracking and collision objectives, i.e., $f = f_{\text{track}} + f_{\text{coll}}$, the printed mechanism failed after one cycle through fracture in one of the flexures. The prototype for which f_{fail} was included in the optimization was able to run for more than an hour (this accounts for more than 2000 motion cycles) without noticing any sign of material failure nor onset of yielding.

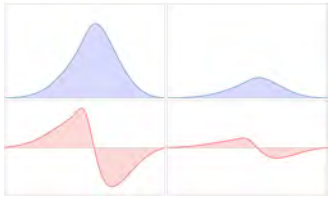

Including additional objectives rather than simply using f_{track} leads to a decrease in tracking accuracy, but as can be seen from Tab. 2 and Fig. 8, the functionality of the mechanism is still maintained. Evaluating the various objectives and their derivatives with respect to the design parameters is not expensive in comparison to the time spent on simulation: given parameter values for the flexures, we compute the equilibrium configuration of the mechanism

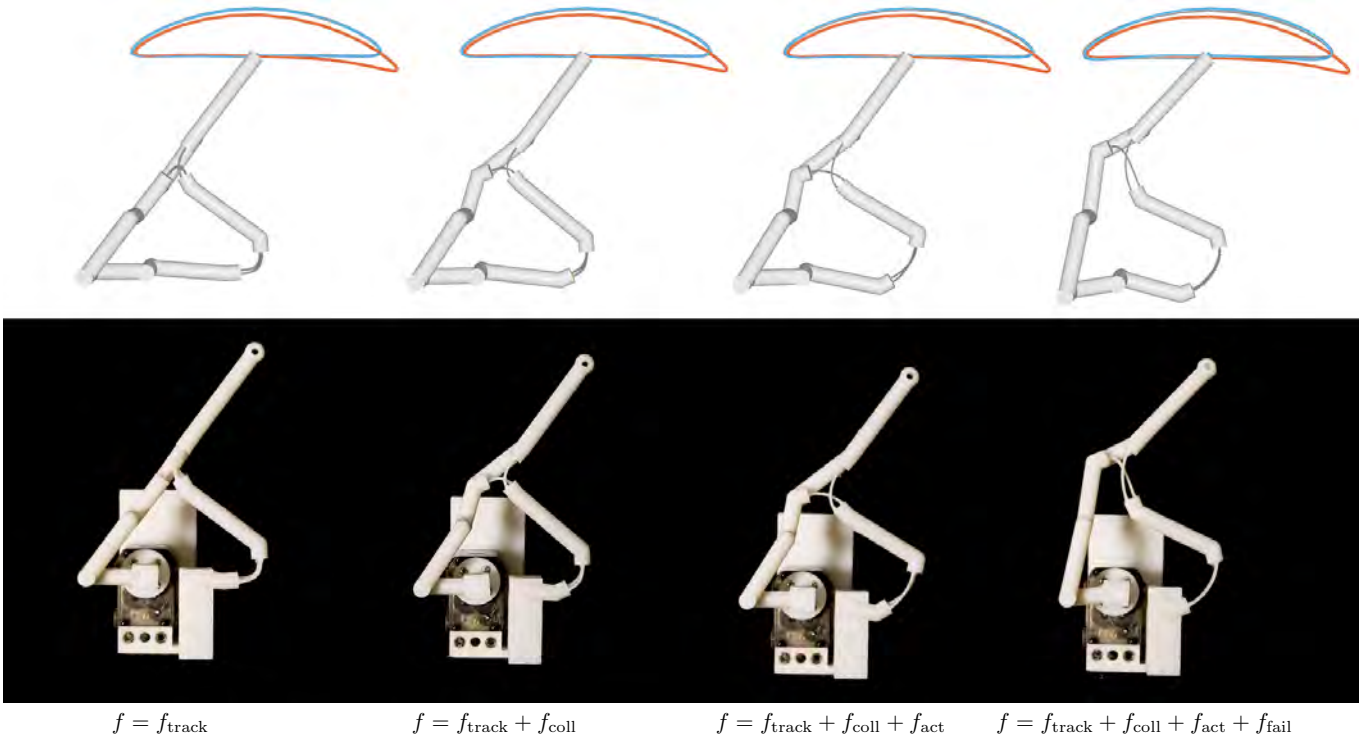

Fig. 8. **Chebyshev Linkage.** Simulated (top row) and fabricated (bottom row) compliant Chebyshev linkages that were optimized with different objective terms as indicated. Starting from the red trajectory after initialization, the trajectory (in blue) of a marker on the original assembly is recovered for all combinations of objectives. However, only with f_{fail} active (right most assembly), the compliant mechanism lasts.

for all 60 steps along the motion cycle, each of which means solving a nonlinear system of equations. Simulation is required at least once per quasi-Newton iteration for solving (17), and potentially more often during line search. Tab. 1 shows a comparison between the time spent on simulation against the time spent on objective evaluation, once using $f = f_{\text{track}} + f_{\text{coll}}$ and once with the addition of our most expensive objective f_{fail}.

Jansen's Linkage. The fundamental building block of Theo Jansen's Strandbeests is a leg mechanism with a total of 9 hinges and 9 rigid links, driven by a single motor. We replaced 8 hinges with layered, compliant designs, two among which are three-way couplings. As can be see in Fig. 9 and the accompanying video, the motion trajectory of the unoptimized mechanism (in red) is far off the original trajectory (in black). With our performance objectives, however, we can recover the function of the mechanism (fraction of the trajectory in contact with the ground, in blue) while keeping the stresses of the leg mechanism within reasonable bounds.

As previously mentioned, we first experimented with CMA-ES due to the complex derivatives of our objectives. With Jansen's leg being one of the most complex examples when it comes to flexure count, it is well-suited for a comparison of a derivative-free optimization (CMA-ES) to our method of choice – a quasi-Newton

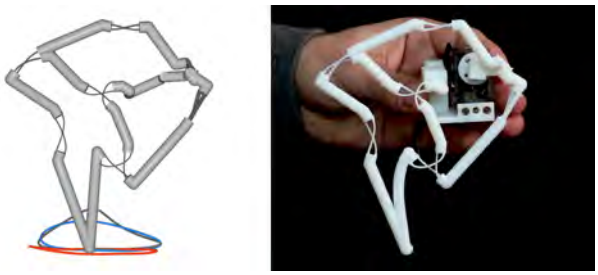

Fig. 9. **Jansen's Linkage.** After replacing conventional hinges with compliant flexures, the end effector trajectory (red) deviates significantly from the original trajectory (in black). After optimally placing, orienting, and sizing the flexures, we can recover the lower portion of the trajectory (in contact with the ground) to a large degree (in blue).

with L-BFGS: after 50 iterations of quasi-Newton with only f_{track} active, the objective value is two orders of magnitude smaller than after the same amount of CMA-ES iterations. We further observe that quasi-Newton moves a subset of parameters such as, e.g., the

	$f_{\text{track}} + f_{\text{coll}}$	$f_{\text{track}} + f_{\text{coll}} + f_{\text{fail}}$
Full iteration	4.82s	5.35s
Simulation	3.63s	3.81s
Objective evaluation	0.037s	0.068s

Table 1. Computation times for optimizing the Chebyshev linkage using different objective terms as indicated in the top row. Simulation is the dominant part in both cases, whereas the evaluation of the objective terms is negligible in comparison.

flexures' cross section parameters significantly more than CMA-ES, suggesting that CMA-ES is ill-suited for the task at hand even if we ignore time complexity.

One quasi-Newton step for the Jansen leg (highest number of flexures) takes on average 39s on a machine with an Intel Core i7-6700 3.5GHz processor with a total of 32 GB of RAM. For improved efficiency, we parallelized evaluations along the trajectory and also along the line search direction. In comparison, one CMA-ES iteration takes on average 31s with objective evaluations parallelized.

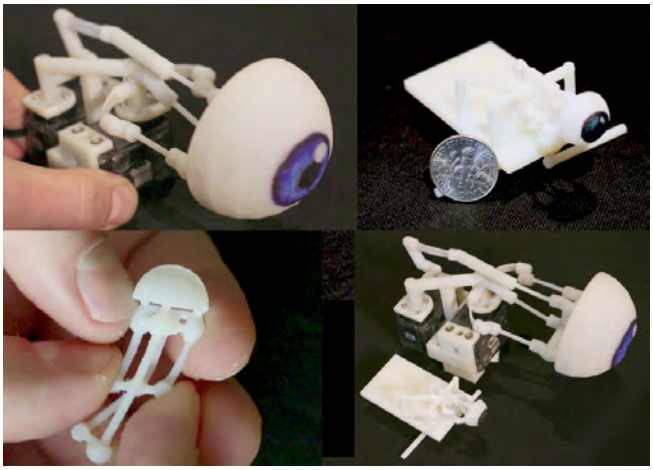

Fig. 10. **Eye Mechanism.** Compliant eye mechanism at human-scale (top left), at Dime-scale (bottom left and top right), and a side-by-side comparison (bottom right).

Eye Mechanism. The design of well-functioning animatronic eye mechanisms at small scales is a formidable task. For our Eye Mechanism, we estimated a fully compliant version from a spatial input with 2 hinges and 4 ball-and-sockets, jointing together a total of 8 rigid links, and driven by two rotational motors. The user starts by specifying motor profiles that lead to eye motion that sufficiently spans the desired range of motion. And as one can see from the accompanying video (see also Fig. 10), the compliant version preserves this range closely, hence, is function-preserving. The eye ball of the input roughly matches the size of a human eye. However, many animals have eyes of far smaller scales: if, e.g., a lizard is replicated as an animatronic, one needs mechanisms that run reliably at very small scales. As we illustrate with a miniaturized eye mechanism (compare with Fig. 10), the use of compliance enables fabrication at scales far beyond what is possible when relying on conventional mechanical assemblies. This is due to the scale invariant minimal tolerance between movable parts (approximately $0.25mm$ for Stratasys' Connex series): as we demonstrate in our video, we had to significantly reduce the range of motion of the ball-and-sockets to prevent balls from popping out of their socket. Hence, the mechanical eye mechanism at Dime-scale is not function-preserving while our compliant version is.

RC Car. For a steering mechanism, function-preservation is pivotal. For our RC CAR, we estimated a compliant version of a conventional steering mechanism consisting of 5 rigid bodies jointed together with 2 hinges and 2 ball-and-sockets, and driven by a single motor. As we demonstrate in our video (see also Fig. 11), the functionality of the original mechanism is preserved, even under self-weight of the car and frictional contact at the three wheel shafts: note how the compliant ball-and-socket flexures are pulling or pushing dependent on the steering direction and do not buckle under compression. Due to symmetry, we optimized only half of the mechanism, then mirrored the resulting monolithic structure prior to fabrication. After adding a servo and an electronic board, we control our compliant car with a cellphone over Bluetooth.

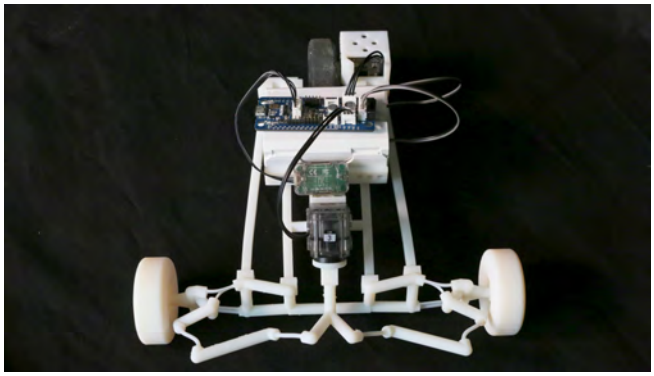

Fig. 11. **RC Car.** Remote controlled car featuring a fully compliant steering mechanism. In addition to preserving the steering functionality of the input mechanism, this design was optimized to sustain its own weight.

Compliant Hand. For our compliant hand design, we replaced all 9 hinges of a conventional finger mechanism (9 hinges, 1 linear actuator, 9 rigid links) with flexures, then optimized the resulting monolithic mechanism for fabrication with Rigur. We then attached 5 identical fingers to a laser-cut piece of Plexiglas and actuated them with strings from a distance (see Fig. 12 and accompanying video for teleoperation footage): by pulling on the strings we store potential energy in the fingers. This energy is released when reducing the actuation forces on the strings, causing the fingers to move back to the rest configuration where the elastic energy is zero.

Dragon. For our dragon, we estimated a compliant version of a spatial wing mechanism (1 motor, 3 hinges, 1 ball-and-socket, 7 rigid links). We replaced all joints but the motor with compliant

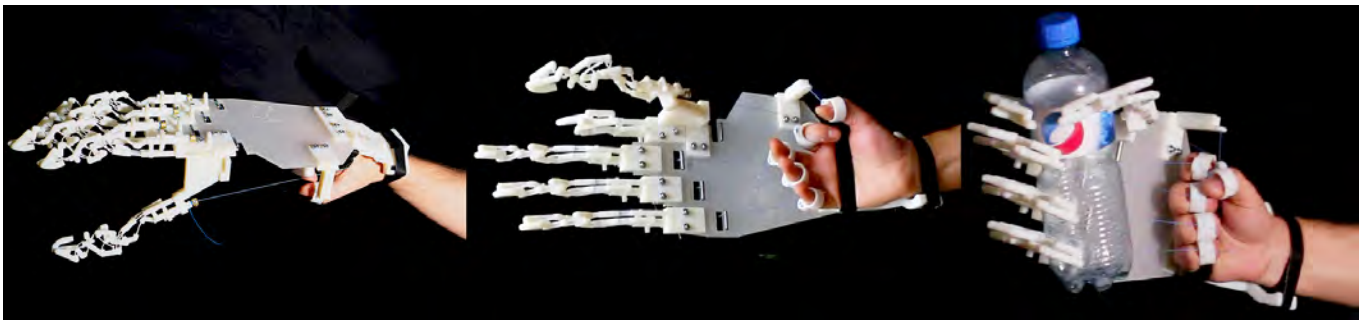

Fig. 12. **Compliant Hand.** A compliant finger mechanism is replicated and assembled to create a fully operational hand. Side and bottom views are shown on the left and in the middle. On the right we show the hand performing a teleoperated grasping task using cables for actuation. Thanks to restoring forces from the compliant flexures, the hand can be actuated using a single cable per finger.

flexures. While seemingly simple, we observe that the hinge flexures undergo twist deformations, underlining the importance of minimizing stresses due to torsion. These twist deformations are due to proximity of two compliant hinges with flexures aligned orthogonally to one another. If only failure prevention for stretching and bending is active, twist stresses are too high for the targeted printer material, and the risk of material failure high. We observe (see accompanying video) that the degrees of freedom of the conventional hinges are not well preserved. Nonetheless, the trajectory of the user-specified marker point is preserved to a high degree, resulting in a function-preserving and failure-resistant compliant wing mechanism with intricate 3D motion. Interestingly, this mechanism is bi-stable as we can see when looking at the energy profile. Besides the rest configuration, there is a stable equilibrium at an intermediate step t along the cyclic motion.

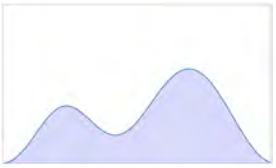

Summary. We used our method to design and fabricate a set of planar and spatial compliant mechanisms showing different types of joints, varying complexity, and diverse functions. Though different, all these examples share the need for explicitly preventing material failure during optimization: all of our tests indicate that when only motion tracking is taken into account, the fabricated mechanism will invariably fail during operation. In contrast, by incorporating a failure-preventing objective in the optimization, we obtain compliant designs with largely improved robustness at the expense of somewhat reduced tracking accuracy. Tab. 2 reports comprehensive performance data for all examples that were fabricated.

Model	# DoF	# It.	Avg. It. Cost (s)	Mean Error (mm)	Max Error (mm)
Chebyshev	35	152	5	0.59	1.04
Jansen	112	880	39	1.67	8.16
Eye	110	283	34	1.65	5.04
Car	63	76	28	0.86	2.35
Hand	141	183	31	0.63	5.28
Dragon	70	164	11	1.15	3.42

Table 2. **Statistics.** The columns (from left to right) list the number of degrees of freedom, the number of iterations required for convergence, the average iteration cost, as well as the mean and maximum error for the motion tracking objective.

6 CONCLUSIONS

We presented a computational tool for designing compliant mechanisms and demonstrated its use on several physical prototypes. While the types of joints supported by our method cover a large range of useful planar and spatial mechanisms, conventional joints performing full revolutions cannot be converted to compliant flexures. However, rather than the result of a specific design tool, this limitation is inherent to compliant mechanisms in general. Fortunately, the number of full-revolution joints is typically small.

In the future, we plan to extend our method to support topology changes. For conventional assemblies, a pivotal requirement is that the degrees of freedom of the joints are equal to the number of unknown state variables at all times, rendering the automated exploration of topological changes an utterly complex task. The use of compliance, however, paves the way for a more graceful exploration of this space thanks to the more even distribution of the infinite stiffness and compliance concentrations of conventional joints. The removal of individual links could make room for overall performance improvements because link-link or link-flexure collisions that prevented further stepping in respective descent directions may no longer be present.

As another limitation, we have so far focused on structurally-sound and function-preserving kinematic behavior. Dynamic effects, however, can play a role as can be observed when teleoperating with our compliant hand. These effects are, however, highly dependent on the choice of material: we sintered an individual finger of our compliant hand and observed a more high-frequent but far less pronounced dynamic behavior. An interesting direction for future work would be to extend our method to model and optimize for these dynamic effects.

Fig. 13. **Dragon.** Full dragon (left) and close-up onto the wing mechanism (right). The wings of the dragon are two identical but mirrored versions of a spatial compliant mechanism. This example exhibits large deformations induced by twist, emphasizing the need for a twist-aware objective for preventing material failure.

If a legged mechanism undergoes a periodic motion, there are at least two stationary points at which the structure is in equilibrium—though one of them (the maximum) is unstable. While we have observed bi-stable behavior in some of our mechanisms (see, e.g., Dragon), designing for multi-stability [Pucheta and Cardona 2010] could be an interesting avenue for further exploration.

Last but not least, there are many interesting applications for compliant mechanisms in the field of robotics, including legged locomotion; see, e.g., [Rutishauser et al. 2008]. We hope that our method can serve as a basis for automating the design process of such compliant legged robots.

REFERENCES

Alejandro E. Albanesi, Victor D. Fachinotti, and Martin A. Pucheta. 2010. A Review on Design Methods for Compliant Mechanisms. *Mecanica Computacional* (2010).

Moritz Bächer, Bernd Bickel, Doug L. James, and Hanspeter Pfister. 2012. Fabricating articulated characters from skinned meshes. *ACM Trans. Graph.* 31, 4, Article 47 (July 2012), 9 pages. https://doi.org/10.1145/2185520.2185543

Moritz Bächer, Stelian Coros, and Bernhard Thomaszewski. 2015. LinkEdit: Interactive Linkage Editing Using Symbolic Kinematics. *ACM Trans. Graph.* 34, 4, Article 99 (July 2015), 8 pages. https://doi.org/10.1145/2766985

Moritz Bächer, Emily Whiting, Bernd Bickel, and Olga Sorkine-Hornung. 2014. Spin-it: Optimizing Moment of Inertia for Spinnable Objects. *ACM Trans. Graph.* 33, 4, Article 96 (July 2014), 10 pages. https://doi.org/10.1145/2601097.2601157

Miklós Bergou, Basile Audoly, Etienne Vouga, Max Wardetzky, and Eitan Grinspun. 2010. Discrete Viscous Threads. *ACM Trans. Graph.* 29, 4, Article 116 (July 2010), 10 pages. https://doi.org/10.1145/1778765.1778853

Miklós Bergou, Max Wardetzky, Stephen Robinson, Basile Audoly, and Eitan Grinspun. 2008. Discrete Elastic Rods. *ACM Trans. Graph.* 27, 3, Article 63 (Aug. 2008), 12 pages. https://doi.org/10.1145/1360612.1360662

Jacques Calì, Dan A. Calian, Cristina Amati, Rebecca Kleinberger, Anthony Steed, Jan Kautz, and Tim Weyrich. 2012. 3D-printing of Non-assembly, Articulated Models. *ACM Trans. Graph.* 31, 6, Article 130 (Nov. 2012), 8 pages. https://doi.org/10.1145/2366145.2366149

Duygu Ceylan, Wilmot Li, Niloy J. Mitra, Maneesh Agrawala, and Mark Pauly. 2013. Designing and Fabricating Mechanical Automata from Mocap Sequences. *ACM Trans. Graph.* 32, 6, Article 186 (Nov. 2013), 11 pages. https://doi.org/10.1145/2508363.2508400

Weikai Chen, Xiaolong Zhang, Shiqing Xin, Yang Xia, Sylvain Lefebvre, and Wenping Wang. 2016. Synthesis of Filigrees for Digital Fabrication. *ACM Trans. Graph.* 35, 4, Article 98 (July 2016), 13 pages. https://doi.org/10.1145/2897824.2925911

Stelian Coros, Bernhard Thomaszewski, Gioacchino Noris, Shinjiro Sueda, Moira Forberg, Robert W. Sumner, Wojciech Matusik, and Bernd Bickel. 2013. Computational Design of Mechanical Characters. *ACM Transactions on Graphics (proceedings of ACM SIGGRAPH)* 32, 4 (2013), to appear.

M. I. Frecker, G. K. Ananthasuresh, S. Nishiwaki, N. Kikuchi, and S. Kota. 1997. Topological Synthesis of Compliant Mechanisms Using Multi-Criteria Optimization. *Journal of Mechanical Design* 2, 119 (Jun 1997), 238–245.

Akash Garg, Andrew O. Sageman-Furnas, Bailin Deng, Yonghao Yue, Eitan Grinspun, Mark Pauly, and Max Wardetzky. 2014. Wire Mesh Design. *ACM Trans. Graph.* 33, 4, Article 66 (July 2014), 12 pages. https://doi.org/10.1145/2601097.2601106

Nikolaus Hansen, Sibylle D. Müller, and Petros Koumoutsakos. 2003. Reducing the Time Complexity of the Derandomized Evolution Strategy with Covariance Matrix Adaptation (CMA-ES). *Evol. Comput.* 11, 1 (March 2003), 1–18. https://doi.org/10.1162/106365603321828970

Jean Hergel and Sylvain Lefebvre. 2015. 3D Fabrication of 2D Mechanisms. In *Computer Graphics Forum*, Vol. 34. Wiley Online Library, 229–238.

Rodney Hill. 1998. *The Mathematical Theory of Plasticity.* Clarendon Press.

Jonathan B. Hopkins and Martin L. Culpepper. 2010a. Synthesis of multi-degree of freedom, parallel flexure system concepts via Freedom and Constraint Topology (FACT) âĂŞ Part I: Principles. *Precision Engineering* 34, 2 (2010), 259 – 270. https://doi.org/10.1016/j.precisioneng.2009.06.008

Jonathan B. Hopkins and Martin L. Culpepper. 2010b. Synthesis of multi-degree of freedom, parallel flexure system concepts via freedom and constraint topology (FACT). Part II: Practice. *Precision Engineering* 34, 2 (2010), 271 – 278. https://doi.org/10.1016/j.precisioneng.2009.06.007

L.L. Howell and A. Midha. 1994. A Method for the Design of Compliant Mechanisms With Small-Length Flexural Pivots. *ASME. J. Mech. Des.* 116, 1 (1994), 280–290.

Larry L. Howell. 2001. *Compliant Mechanisms.* Wiley-Interscience.

Larry L. Howell, Spencer P. Magleby, and Brian M. Olsen. 2013. *Handbook of Compliant Mechanisms.* Wiley.

Zhen Huang, Qinchuan Li, and Huafeng Ding. 2013. *Basics of Screw Theory.* Springer Netherlands, Dordrecht, 1–16. https://doi.org/10.1007/978-94-007-4201-7_1

Bongjin Koo, Wilmot Li, JiaXian Yao, Maneesh Agrawala, and Niloy J. Mitra. 2014. Creating Works-like Prototypes of Mechanical Objects. *ACM Trans. Graph.* 33, 6, Article 217 (Nov. 2014), 9 pages. https://doi.org/10.1145/2661229.2661289

Sridhar Kota and GK Ananthasuresh. 1995. Designing compliant mechanisms. *Mechanical Engineering-CIME* 117, 11 (1995), 93–97.

Sridhar Kota, Jinyong Joo, Zhe Li, Steven M. Rodgers, and Jeff Sniegowski. 2001. Design of Compliant Mechanisms: Applications to MEMS. *Analog Integr. Circuits Signal Process.* 29, 1-2 (Oct. 2001), 7–15. https://doi.org/10.1023/A:1011265810471

L.D. Landau, L.P. Pitaevskii, A.M. Kosevich, and E.M. Lifshitz. 1986. *Theory of Elasticity.* Elsevier. 38 – 86 pages.

Padmanabh Limaye, G. Ramu, Sindhuja Pamulapati, and G.K. Ananthasuresh. 2012. A compliant mechanism kit with flexible beams and connectors along with analysis and optimal synthesis procedures. *Mechanism and Machine Theory* 49 (2012), 21 – 39. https://doi.org/10.1016/j.mechmachtheory.2011.07.008 https://www.youtube.com/watch?v=HuOEG5FqTAE.

Minmin Lin, Tianjia Shao, Youyi Zheng, Niloy J. Mitra, and Kun Zhou. 2016. Recovering Functional Mechanical Assemblies from Raw Scans. *Transactions on Visualization*

and Comptuer Graphics (2016).

Lin Lu, Andrei Sharf, Haisen Zhao, Yuan Wei, Qingnan Fan, Xuelin Chen, Yann Savoye, Changhe Tu, Daniel Cohen-Or, and Baoquan Chen. 2014. Build-to-last: Strength to Weight 3D Printed Objects. *ACM Trans. Graph.* 33, 4, Article 97 (July 2014), 10 pages. https://doi.org/10.1145/2601097.2601168

Eder Miguel, Mathias Lepoutre, and Bernd Bickel. 2016. Computational Design of Stable Planar-rod Structures. *ACM Trans. Graph.* 35, 4, Article 86 (July 2016), 11 pages. https://doi.org/10.1145/2897824.2925978

Niloy J. Mitra, Yong-Liang Yang, Dong-Ming Yan, Wilmot Li, and Maneesh Agrawala. 2010. Illustrating How Mechanical Assemblies Work. *ACM Trans. Graph.* 29, 4, Article 58 (July 2010), 12 pages. https://doi.org/10.1145/1778765.1778795

Yuki Mori and Takeo Igarashi. 2007. Plushie: An Interactive Design System for Plush Toys. *ACM Trans. Graph.* 26, 3, Article 45 (July 2007). https://doi.org/10.1145/1276377.1276433

Przemyslaw Musialski, Thomas Auzinger, Michael Birsak, Michael Wimmer, and Leif Kobbelt. 2015. Reduced-Order Shape Optimization Using Offset Surfaces. *ACM Transactions on Graphics (ACM SIGGRAPH 2015)* 34, 4 (Aug. 2015), to appear–9. http://www.cg.tuwien.ac.at/research/publications/2015/musialski-2015-souos/

Jorge Nocedal. 1980. Updating quasi-Newton matrices with limited storage. *Mathematics of computation* 35, 151 (1980), 773–782. https://doi.org/10.1090/S0025-5718-1980-0572855-7

Jesús Pérez, Bernhard Thomaszewski, Stelian Coros, Bernd Bickel, José A. Canabal, Robert Sumner, and Miguel A. Otaduy. 2015. Design and Fabrication of Flexible Rod Meshes. *ACM Trans. Graph.* 34, 4, Article 138 (July 2015), 12 pages. https://doi.org/10.1145/2766998

Romain Prévost, Emily Whiting, Sylvain Lefebvre, and Olga Sorkine-Hornung. 2013. Make It Stand: Balancing Shapes for 3D Fabrication. *ACM Transactions on Graphics (proceedings of ACM SIGGRAPH)* 32, 4 (2013), to appear.

MartÃŋn A. Pucheta and Alberto Cardona. 2010. Design of bistable compliant mechanisms using precisionâĂŞposition and rigid-body replacement methods. *Mechanism and Machine Theory* 45, 2 (2010), 304 – 326. https://doi.org/10.1016/j.mechmachtheory.2009.09.009

S. Rutishauser, A. Sproewitz, L. Righetti, and A. J. Ijspeert. 2008. Passive compliant quadruped robot using central pattern generators for locomotion control. *International Conference on Biomedical Robotics and Biomechatronics* (2008).

Christian Schüller, Daniele Panozzo, Anselm Grundhöfer, Henning Zimmer, Evgeni Sorkine, and Olga Sorkine-Hornung. 2016. Computational Thermoforming. *ACM Trans. Graph.* 35, 4, Article 43 (July 2016), 9 pages. https://doi.org/10.1145/2897824.2925914

Mélina Skouras, Bernhard Thomaszewski, Stelian Coros, Bernd Bickel, and Markus Gross. 2013. Computational Design of Actuated Deformable Characters. *ACM Transactions on Graphics (proceedings of ACM SIGGRAPH)* 32, 4 (2013), to appear.

Mélina Skouras, Bernhard Thomaszewski, Peter Kaufmann, Akash Garg, Bernd Bickel, Eitan Grinspun, and Markus Gross. 2014. Designing Inflatable Structures. *ACM Trans. Graph.* 33, 4, Article 63 (July 2014), 10 pages. https://doi.org/10.1145/2601097.2601166

Stuart T. Smith. 2000. *Flexure: Elements of Elastic Mechanuisms.* CRC Press.

Ondrej Stava, Juraj Vanek, Bedrich Benes, Nathan Carr, and Radomír Měch. 2012. Stress relief: improving structural strength of 3D printable objects. *ACM Trans. Graph.* 31, 4, Article 48 (July 2012), 11 pages. https://doi.org/10.1145/2185520.2185544

Bernhard Thomaszewski, Stelian Coros, Damien Gauge, Vittorio Megaro, Eitan Grinspun, and Markus Gross. 2014. Computational Design of Linkage-based Characters. *ACM Trans. Graph.* 33, 4, Article 64 (July 2014), 9 pages. https://doi.org/10.1145/2601097.2601143

Nobuyuki Umetani, Yuki Koyama, Ryan Schmidt, and Takeo Igarashi. 2014. Pteromys: Interactive Design and Optimization of Free-formed Free-flight Model Airplanes. *ACM Trans. Graph.* 33, 4, Article 65 (July 2014), 10 pages. https://doi.org/10.1145/2601097.2601129

Nobuyuki Umetani, Athina Panotopoulou, Ryan Schmidt, and Emily Whiting. 2016. Printone: Interactive Resonance Simulation for Free-form Print-wind Instrument Design. *ACM Trans. Graph.* 35, 6, Article 184 (Nov. 2016), 14 pages. https://doi.org/10.1145/2980179.2980250

Nobuyuki Umetani and Ryan Schmidt. 2013. Cross-sectional Structural Analysis for 3D Printing Optimization. In *SIGGRAPH Asia 2013 Technical Briefs (SA '13).* ACM, New York, NY, USA, Article 5, 4 pages. https://doi.org/10.1145/2542355.2542361

Michael Yu Wang and Shikui Chen. 2009. Compliant Mechanism Optimization: Analysis and Design with Intrinsic Characteristic Stiffness. *Mechanics Based Design of Structures and Machines* 37, 2 (2009), 183–200. https://doi.org/10.1080/15397730902761932 arXiv:http://dx.doi.org/10.1080/15397730902761932

Jonas Zehnder, Stelian Coros, and Bernhard Thomaszewski. 2016. Designing Structurally-sound Ornamental Curve Networks. *ACM Trans. Graph.* 35, 4, Article 99 (July 2016), 10 pages. https://doi.org/10.1145/2897824.2925888

Qingnan Zhou, Julian Panetta, and Denis Zorin. 2013. Worst-case structural analysis. *ACM Trans. Graph.* 32, 4, Article 137 (July 2013), 12 pages.

Lifeng Zhu, Weiwei Xu, John Snyder, Yang Liu, Guoping Wang, and Baining Guo. 2012. Motion-guided Mechanical Toy Modeling. *ACM Trans. Graph.* 31, 6, Article 127 (Nov. 2012), 10 pages. https://doi.org/10.1145/2366145.2366146